Gradient fluoride, Zn-salt-rich hydrophobic interphase enabled by Zn-philic, H_2O-phobic, anion-philic polymer "skin" for anode-free solid Zn battery

Xinpeng Han,[a] Jinpeng Han,[c*] Kang Ma,[a] Jiaqi Wen,[b] Lianpeng Li,[a] Daliang Han,[b] Jie Sun,[a,d*]

[a]School of Chemical Engineering and Technology, Tianjin University, Tianjin 300072, China
Dr. X. Han, Mr. K. Ma, Mr. L. Li and Prof. J. Sun.

[b]Nanoyang Group, Tianjin Key Laboratory of Advanced Carbon and Electrochemical Energy Storage, School of Chemical Engineering and Technology, and Collaborative Innovation Center of Chemical Science and Engineering (Tianjin), Tianjin University, Tianjin, 300072, China
Mr. J. Wen and Prof. D. Han.

[c] Zhejiang University, Hangzhou, China
Dr. J. Han.

[d]Quzhou Institute for Innovation in Resource Chemical Engineering, No. 78, Jiuhuabei Avenue, Quzhou City, Zhejiang Province, China
Prof. J. Sun.

E-mail: jies@tju.edu.cn, jinpeng.han@zju.edu.cn

Table of Contents

1. Discussion S1: the novelty of our work……..…..…….…..…...S3-S5
2. Experimental procedures ……..……..…..……..…..……S6
3. Results and discussions ……..……...……...……..…..……..…..S7-S55
4. References..……..…..……..……..…..……. .. S56

Discussion S1: the novelty of our work

In this work, the in-depth SEI composition-property-performance relationship was investigated to construct a unique SEI layer with the gradient distribution of zinc salts-rich-inorganic nanoparticles (*e.g.*, ZnF_2, ZnS, $ZnSO_3$, and ZnO). Unlike previous studies that mainly focused on the determination of new zinc salts-rich-inorganic phases in SEI (*Nat. Commun.,* 2023, 14, 5443; *Energy Environ. Sci.,* 2024, 17, 680), we proposed that the rational design of gradient zinc salts-rich-inorganic nanoparticle distribution could deliver the unprecedented electrochemical performances (**Fig. 3**-**5**). Specifically, in our SEI, the amounts of ZnF_2 near Zn electrode were higher than those near SPE moiety, which was demonstrated by the high-resolution TEM (HRTEM) images and the X-ray photoelectron spectroscopy (XPS) of SEI layer. The number ratios of ZnF_2/ZnO nanoparticles in our SEI were higher than those in 1M $Zn(OTf)_2$-H_2O-derived SEI, which was proved by the XPS element analysis of SEI layer with a dynamic etching process. Considering the higher dendrite-suppressing ability of ZnF_2 instead of ZnO (*Adv. Mater.* **2023**, 35, 2207908), our SEI could exhibit the stronger capability in suppressing the growth of Zn dendrite. Compared with ZnO, ZnF_2 showed the higher desolvation ability to restrain possible side reactions as indicated by the molecular dynamic (MD) simulations. Owing to the unique distribution of inorganic salts in SEI, the highest mechanical properties of our SEI were achieved compared with the previously reported results (*Adv. Mater.* **2023**, 35, 2210051; *Energy Storage Mater.* **2023**, 59, 102769; *Angew. Chem. Int. Ed.* **2023**, 62, e202311268; *Energy Environ. Sci.* **2024**, 17, 680; *Small Methods* **2023**, 7, 2300546; *SmartMat* **2024**, 5, e1212; *ACS Nano* **2024**, 18, 3752). Hence, our designed SEI could inhibit the external stress originating from dendritic growth and the undesirable volume expansion of Zn anode, thus tackling the side reactions and high thermodynamic instability of Zn-metal anode.

In addition, the formation mechanism of the unique SEI was attributed to the deep decomposition of Zn-philic, H_2O-phobic contact ion pair (CIP)/aggregate (AGG)-rich electrolyte in the polymer-based electrolyte environment. In previous studies, the formation of organic-rich SEI was mainly attributed to the interfacial evolution of inorganic-rich components with the help of electrolyte solvent molecules (*Adv. Funct. Mater.* **2022**, 32, 2111074; *Angew. Chem. Int. Ed.* **2021**, 60, 13035). In this work, the Zn-philic, H_2O-phobic CIP/AGG-rich electrolyte significantly activated the anion activity and promoted gradient and dense distribution of ZnF_2 components instead of ZnO in SEI. As shown in **Fig. 2E**, the Raman regions (1020~1050 cm^{-1}) reflected the aggregation behavior of OTf^- *via* recording sulfonyl group ($–SO_3$) stretching bands in various electrolytes, in which the three major bands at 1028, 1032.5, and 1037 cm^{-1} attributed to free anions (FA), solvent-separated ion pairs (SSIP, Zn^{2+}-H_2O-OTf^-), and contact ion pairs (CIP, Zn^{2+}-OTf^-)/aggregation (AGG, Zn^{2+}-OTf^--Zn^{2+}), respectively (*Chem. Sci.* **2021**, 12, 5843; *Energy Storage Mater.* **2022**, 47, 203; *Adv. Energy Mater.* **2023**, 13, 2203729). This result demonstrated that OTf^- with a SSIP configuration was predominantly observed in 1 M $Zn(OTf)_2$-H_2O and unpolymerized $Zn(OTf)_2$-H_2O/MPTS solutions, however, OTf^- with a CIP/AGG configuration was proved in our polymer-based electrolyte environment. Since the solvation structure transformation was beneficial for the reduction decomposition of anion complexes, the strong coordination between the OTf^- and Zn^{2+} in a CIP/AGG configuration would promote the formation of an inorganic salt-rich SEI on the Zn anode. As a contrast, SSIP-dominated H_2O-derived solvation sheath would preferentially be decomposed to construct a loose layer in 1 M $Zn(OTf)_2$-H_2O electrolyte, which led to the low reversibility of Zn plating/stripping and rapid generation of the byproduct.

In regard to electrolyte design, previous studies mainly focused on supressing free H_2O activity in electrolytes through the rational molecular design, the formation of polymer electrolyte or H_2O-lean hydrogel, and the generation of hydrophobic and stable interphase (**Table S1**). In this work, two common strategies including rational molecular design (incorporating Zn ion conducting groups such as C=O and hydrophobic groups such as O-Si-CH_3 group to preclude the solvated H_2O erosion) and the formation of H_2O-phobic polymer electrolyte (restraining H_2O-related side reactions) and one unique strategy (the construction of CIP/AGG-rich electrolyte structure) were rationally integrated for electrolyte design (**Fig. 1**). In this work, the Zn-philic, H_2O-phobic CIP/AGG-rich electrolyte significantly activated the anion activity and promoted gradient and dense distribution of ZnF_2 components instead of ZnO in SEI. Owing to the unique electrolyte design, a unique SEI layer with the gradient distribution of zinc salts-rich-inorganic nanoparticles (*e.g.*, ZnF_2, ZnS, $ZnSO_3$, and ZnO) was constructed. Hence, at high depth of discharge of 34.2%, the symmetric cell maintained long-term stability for over 1000 h. Impressively, anode-free battery delivered superior performance with a high capacity retention of 99.2% after 110 cycles. **Notably, solid zinc ion batteries (ZIBs) with such low N/P ratios and even anode-free ZIBs are firstly reported in our work** (**Table S1**).

Table S1 The advantages of our design strategy.

Adoptinig Strategies	Performances of Zn battery with low N/P ratio	Interfacial analysis	References
Ex-situ polymerization	Solid Zn ion battery (No N:P ratio)	No interfacial analysis	*Adv.Mater.,* 2015, 27, 5617
Rational molecular design	Solid Zn ion battery (No N:P ratio)	No interfacial analysis	*Energy Environ. Sci.,* 2018, 11, 941
Rational molecular design and *in-situ* polymerization	Solid Zn ion battery (No N:P ratio)	No interfacial analysis	*Small,* 2020, 16, 2002528
Rational molecular design and *ex-situ* polymerization	Solid Zn ion battery (No N:P ratio)	No interfacial analysis	*ACS Appl. Mater. Inter.,* 2021, 13, 36320
Rational molecular design and *ex-situ* polymerization	Liquid Zn ion battery (No N:P ratio)	No interfacial analysis	*Energy Environ. Sci.,* 2021, 14, 3492
Rational molecular design and *ex-situ* polymerization	Solid Zn ion battery (No N:P ratio)	No interfacial analysis	*Adv.Mater.* 2022, 34, 2207682
Break the hydrogen bond between H_2O molecules and formation of hydrogel	Solid Zn ion battery (No N:P ratio)	No interfacial analysis	*Adv.Mater.* 2022, 34, 2110140
In-situ polymerization induced well-bonded and H_2O-poor interface	Solid Zn ion battery (No N:P ratio)	No interfacial analysis	*Adv.Mater.* 2022, 34, 2207118
Rational molecular design	Solid Zn ion battery (No N:P ratio)	No interfacial analysis	*ACS Appl. Mater.Inter., 2023, 15, 6839*
Lean-water hydrogel with rational molecular design	Solid Zn ion battery (No N:P ratio)	No interfacial analysis	*Nat. Commun*. 2023, 14, 3890
Rational molecular design and *in-situ* polymerization	Solid Zn ion battery (No N:P ratio)	ZnF_2, ZnS and zinc borate-based SEI	*Angew. Chem. Int. Ed.,* 2020, 59, 23836
Rational molecular design and *ex-situ* polymerization	Solid Zn ion battery (No N:P ratio)	ZnF_2/ZnO/ZnS-based SEI	*Adv. Funct. Mater.* 2022, 32, 2207909
"Polymer-in-salt" electrolyte to enhance the chain activity	Solid Zn ion battery (No N:P ratio)	ZnF_2-rich inorganic/organic hybrid SEI	*Adv. Funct. Mater.*2024,34, 2307740
Rational molecular design	Liquid Zn ion battery (No N:P ratio)	No interfacial analysis	*Nano Energy,* 2022, 99, 107426
Zn-philic, H_2O-phobic additive	Liquid Zn ion battery (No N:P ratio)	ZnF_2/$ZnCO_3$/sulfide-based SEI	*Adv. Funct. Mater.* 2022, 32, 2209642
CIP/AGG-rich solvation sheath	Liquid Zn ion battery (No N:P ratio)	Zn_xNO_y/$ZnSO_3$/ZnS-based SEI	*ACS Energy Lett.* 2022, 7, 4459
Regulation of solvation sheath	Liquid Zn ion battery with N:P of 2.3	ZnS/ZnS-based SEI	*Angew. Chem. Int. Ed.* 2022, 61, e202212839
Hydrophobic interphase through regulation of solvation sheath	Liquid Zn ion battery with N:P of 0	No interfacial analysis	*J.Am.Chem.Soc.* 2022, 144, 7160
CIP/AGG-rich solvation sheath	Liquid Zn ion battery with N:P of 1.8	ZnF_2/ZnS/ZnO-based SEI	*Angew. Chem. Int. Ed.* 2023, 62, e202310290
CIP/AGG-rich solvation sheath	Liquid Zn ion battery (No N:P ratio)	ZnF_2/$Zn_3(PO_4)_2$-based SEI	*Nat. Commun*. 2023, 14, 5443
Hydrophobic interphase through H_2O-poor counter-ion solvation sheath	Liquid Zn ion battery with N:P of 1.5	Inorganic-rich inner SEI and organic-rich outer SEI	*Angew. Chem. Int. Ed.* 2024, 63, e202318063
Rational molecular design,	Solid Zn ion battery with	Gradient fluoride, Zn-salt-	Our work

in-situ interfacial polymerization-derived Zn-philic, H_2O-phobic "skin" and CIP/AGG-rich electrolyte structure	N:P of 0	rich SEI with an unprecedented average modulus of 71.25 GPa

Note: (black color: solid Zn battery, blue color: liquid Zn battery, Red color: Our solid Zn battery)

Experimental Procedures

In-situ synthesis of poly(3-methacryloxypropyl trimethoxysilane) (PMPTS)-based solid polymer electrolyte (SPE) and Se/pPAN

The molar ratio of $Zn(OTf)_2$:3-methacryloxypropyl trimethoxysilane (MPTS):H_2O was 1.2:1:13.2. $Zn(OTf)_2$-H_2O electrolyte was mixed with MPTS solution and thermal initiator (AIBN) to obtain the electrolyte precursor. The mass ratio of AIBN:MPTS was 1wt.%. Then, the electrolyte precursor was dropped on the glass fiber, and which was utilized to assemble the battery. The battery was heated at 60 °C and in-situ polymerization of PMPTS-based SPE was realized. This SPE is a gel electrolyte.
Selenium (99.9%, Aladdin) and polyacrylonitrile (PAN with a chemical formula of $(C_3NH_3)_n$, Sigma-Aldrich) with weight ratio of 8:1 were loaded into a 50 mL zirconium oxide bowl containing zirconium oxide balls and ball-milled at a rotation of 350 rpm for 1 h under room temperature on a planetary ball mill. The obtained uniform mixtures were sealed in a glass vessel and heated at 450°C for 10 hours in N_2 atmosphere. After the temperature is decreased below 50°C, Se/pPAN was gained.

Materials characterization and electrochemical measurements

The microstructures were characterized using a scanning electron microscope (SEM). X-ray diffraction (XRD) analysis was performed on a Bruker D8-Focus diffractometer with Cu Kα radiation (λ = 0.154 nm). Electrolyte property was tested by Raman.
The Fourier transform infrared (FTIR) was used to analyze the change of C=C before and after polymerization.
To determine the composition of SEI layer of Zn anode, XPS was carried out on a Kratos-Axis spectrometer with monochromatic Al Kα (1,486.71 eV) radiation. The cycled Zn anode was washed by H_2O and then dried for half a day.
Nanoindentation (Agilent, G200) was carried out to test the modulus and hardness of SEI layer of cycled Zn metal.
The thickness, composition and distribution of SEI layer were characterized by focused ion beam (FIB, FEI Quata 3D FEG). Using ion beam, the cycled Zn metal electrode was etched. A 5-micron thick Zn electrode micrometer cubic block was longitudinally excavated and transferred to a copper mesh. The ion beam was used to etch and thin it for high-power transmission electron microscope (TEM) observation of the SEI layer.
The electrochemical measurements of symmetrical coin cells were conducted using CR2032 coin cells. The zinc (Zn) metal (50 μm in thickness) was used as both working electrode and counter electrode, and the cells were assembled. The PMPTS-based SPE was in-situ synthesized and used as both the separator and electrolyte for Zn||PMPTS-based SPE||Zn. And the baseline electrolyte was composed of $Zn(OTf)_2$, MPTS and H_2O. The liquid electrolyte was 1M $Zn(OTf)_2$-H_2O, which was composed of $Zn(OTf)_2$ and H_2O. The Whatman GF/D glass fibers was used as separator for Zn||liquid electrolyte||Zn and Zn||baseline electrolyte||Zn coin cell. The in-situ electrochemical impedance spectroscopy (EIS) analysis was tested using the Bio-Logic EC-Lab software.
The ionic conductivity of the PMPTS-based SPE was measured using electrochemical impedance spectroscopy (EIS) at electrochemical workstation, based on the cell of stainless steel||PMPTS-based SPE||stainless steel (SS||PMPTS-based SPE||SS). The electrochemical window of PMPTS-based SPE was studied by linear sweep voltammetry (LSV), in which stainless steel was used as the working electrode and Zn foil as counter and reference electrodes. An electrochemical workstation was used to record the LSV curve at a scanning rate of 0.5 mV s^{-1}.
The electrochemical performance of full cell was tested by using commercial V_2O_5 as cathode (Guangdong Canrd Technology Co. Ltd.) and Zn metal as anode. The Zn anode was covered by PMPTS-based SPE. The glass fiber with an addition of $Zn(OTf)_2$-H_2O electrolyte was pressed onto the PMPTS-based SPE. Then V_2O_5 electrode was pressed onto this glass fiber. The V_2O_5, conductive Super P and polymer binder (PVDF) were mixed and uniformly ground in a ratio of 8:1:1. The NMP solvent was added and mixed to form a slurry. It was then uniformly coated on the surface of the Ti foil and dried under vacuum at 70 °C. The as-fabricated V_2O_5 electrode was used as cathode. The Se/pPAN, conductive Super P and PVDF were mixed and uniformly ground in a ratio of 8:1:1. These mixtures were coated onto the stainless steel. The anode-free full cell using Se/pPAN coated stainless steel as anode and $Zn_xV_2O_5$ as cathode is tested as well. Specifically, the Zn//V_2O_5 full cell is galvanostatically tested for 100 cycles at 100 mA g^{-1}. During the cycling process, the V_2O_5 is activated. Then the battery is disassembled. The electrode is washed with H_2O for three times and dried at room temperature. Afterwards, the obtained cycled $Zn_xV_2O_5$ cathode is utilized for assembling the anode-free battery. The large-size pouch cell is designed to drive the car. The active material is V_2O_5 and the load mass is 4-6 mg cm^{-2}. The parameter of electrode is 8 cm × 12 cm. The SPE is used 10 cm × 14 cm glass fiber and the reaction solution is 2.8 mL. The polymer-based electrolyte is generated through *in-situ* polymerization. The electrochemical performance of pouch cell is tested as well. The detailed fabrication steps of tested pouch cell are as follows: the pouch cell is prepared using a layer-to-layer structure (nine pieces of V_2O_5 cathode and ten pieces of Zn anode). Both the cathode and the Zn anode are in size of 5 × 5 cm^{-2}. Stainless steel foils (1 × 4 cm^{-2}) are connected with the current collector to serve as tabs. Following lamination, the assembled battery is encapsulated within an aluminum-plastic film.

Computational details

DFT calculations were performed using the DMol^3 module in Materials Studio from Accerlrys, Inc.[1] In detail, information on the energy of $[Zn\text{-}solvent_x]^{2+}$ complexes (solvent: H_2O and MPTS) was predicted using the Materials Studio platform. This calculation is based on density functional theory (DFT), using the Perdew-Burke-Ernzerhof (PBE) exchange-correlation functional[2] in the framework of the general gradient approximation (GGA). The stable chemical structures of all $[Zn\text{-}solvent_x]^{2+}$ complexes were optimized based on the same method. An all-electron double numerical basis set with polarization functions (DNP basis set) was used in this contribution. The convergence criteria applied for geometry optimizations were 1.0×10^{-5} au, 2.0×10^{-3} au $Å^{-1}$, and 5.0×10^{-3} Å for energy change, maximum force and maximum displacement, respectively. Based on the calculated energies of molecules, solvation energy was obtained using the following definition: $E_{sol,x} = E_{[Zn\text{-}solventx]2+} - x \times E_{solvent} - E_{Zn2+}$. Here, E_{Zn2+}, $E_{solvent}$ and $E_{[Zn\text{-}solventx]2+}$ represent the energy of Zn^{2+}, the isolated solvent molecule and $[Zn\text{-}solvent_x]^{2+}$ complex, respectively.
The MD simulations were performed using the Forcite module in Materials Studio. A condensed-phase optimized molecular potentials for atomistic simulation studies (COMPASS II) force field was selected to construct the electrolyte system. Hence, SPE contained 120 $Zn(OTf)_2$, 1320 H_2O, 100 MPTS. The 10 MPTS with 10 repeated units was built to represent the polymer. 1M $Zn(OTf)_2$-H_2O contained 20 $Zn(OTf)_2$ and 1120 H_2O. The time step was 1 fs. These two models were equilibrated in the isothermal-isobaric ensemble (constant NPT) to maintain the pressure of 0.1 GPa with a decay constant of 0.1 ps for 200 ps. The temperature was 298 K with Nose thermostat. Then, the productions run of 200 ps were collected in the canonical ensemble (NVT) at 298 K.

Results and discussions

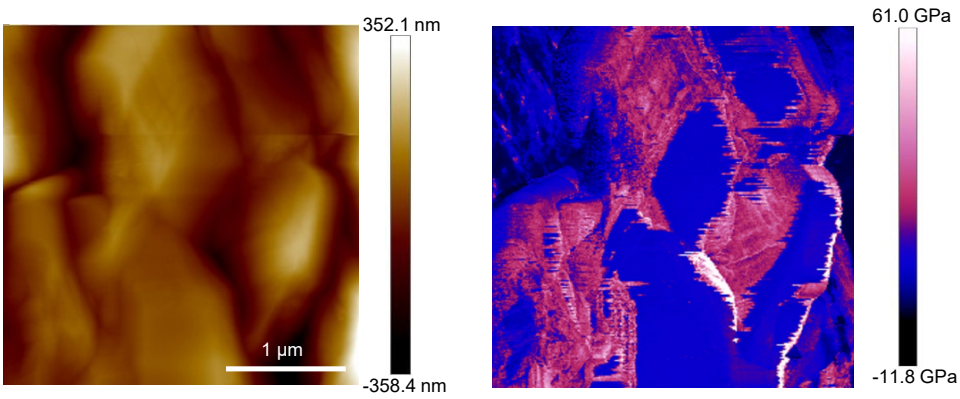

Figure S1. AFM and Young's modulus of deposited Zn dendrite on the Ti foil.

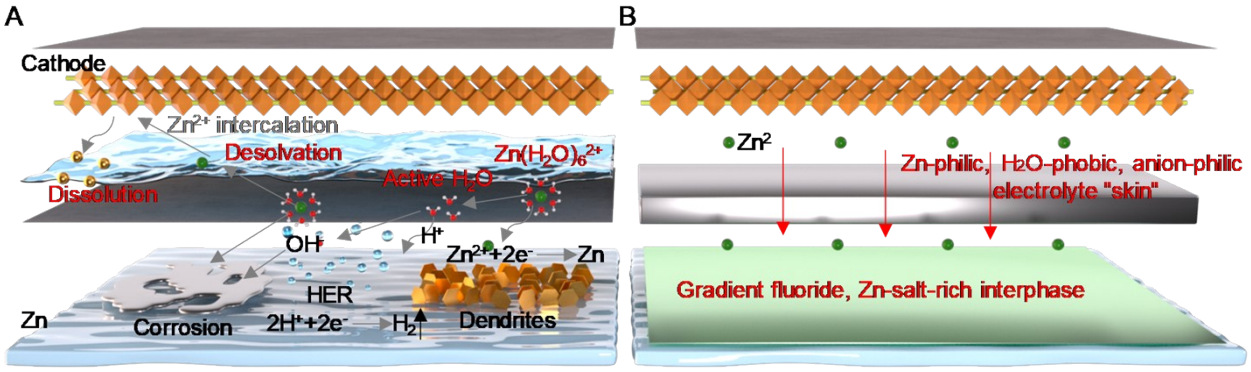

Figure S2. A) Challenges of Zn anode and cathode in aqueous electrolytes. B) Alleviating H_2O-related challenges through *in-situ* designing Zn-philic, H_2O-phobic, anion-philic electrolyte "skin".

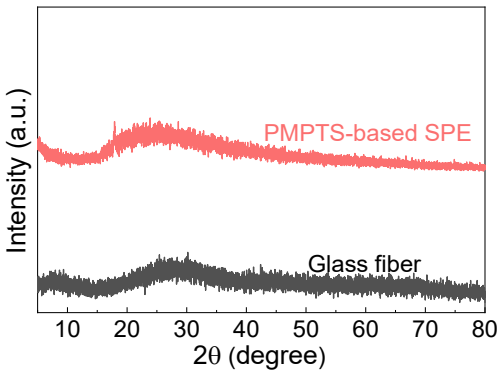

Figure S3. XRD result of glass fiber and PMPTS-based SPE.

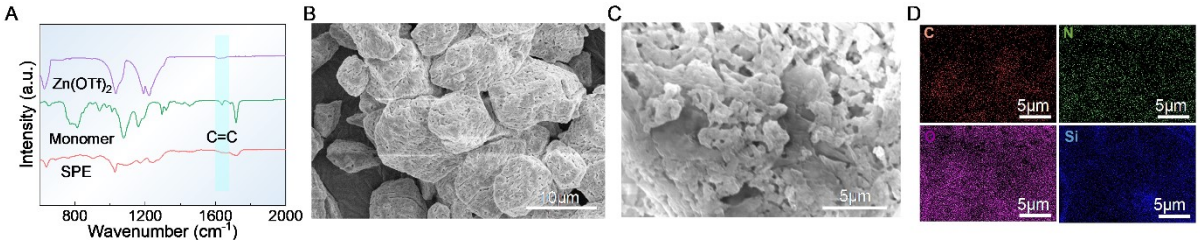

Figure S4. A) FTIR of SPE. B) SEM of PMPTS-based SPE, which is polymerized on the surface of stainless steel. C-D) SEM and EDS mapping of PMPTS-based SPE, which is polymerized on the surface of glass fiber.

Fig. S4B depicts the morphology of SPE, which is formed on the surface of stainless steel foil. The resulted SPE shows porous structure which are beneficial for the transportation of Zn ions. **Fig. S4C** depicts the surface morphology and structure of the PMPTS-based SPE membrane on the surface of glass fiber. The element mapping images confirm the relatively homogeneous distribution of C, N, O, and Si elements in the PMPTS-based SPE membrance (**Fig. S4D**).

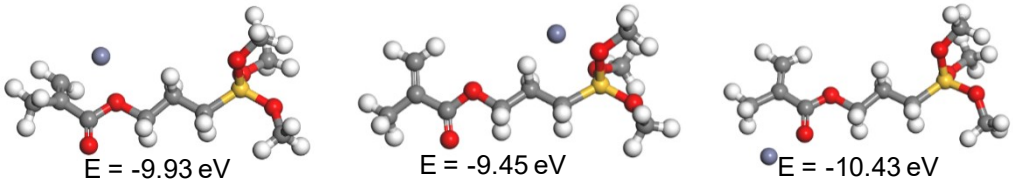

Figure S5. The coordination structures of Zn ion-MPTS.

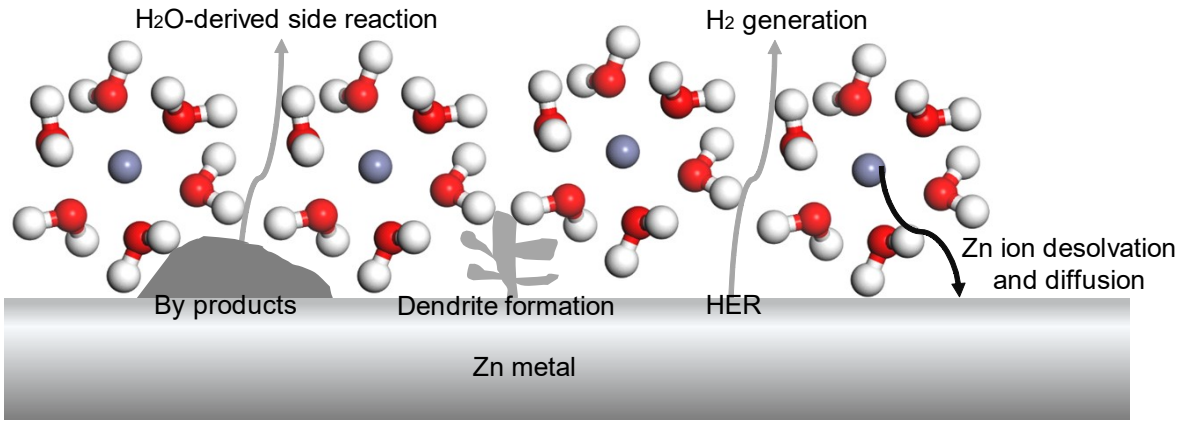

Figure S6. Technical challenges of aqueous Zn anode.

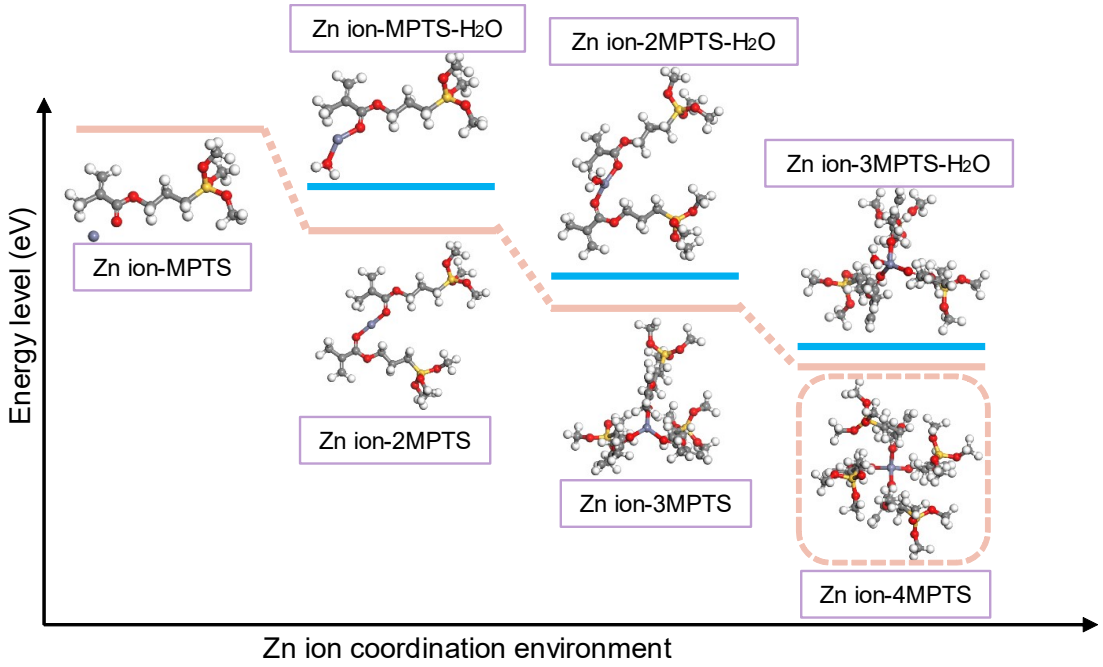

Figure S7. The optimized solvation sheath of Zn ion-MPTS complex.

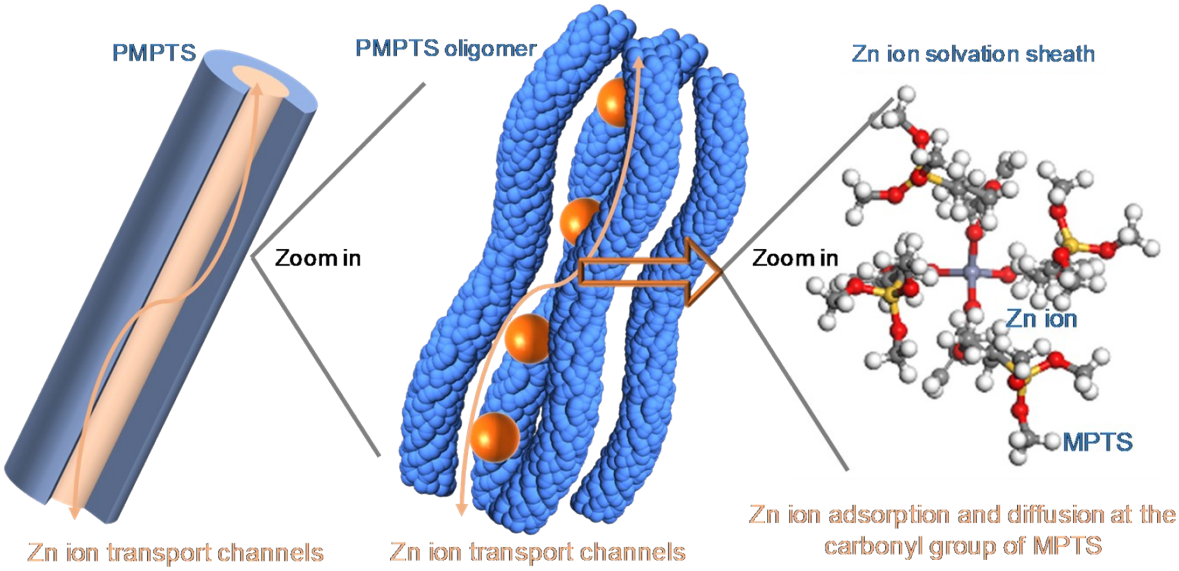

Figure S8. Zn ion adsorption and diffusion at the carbonyl group of PMPTS.

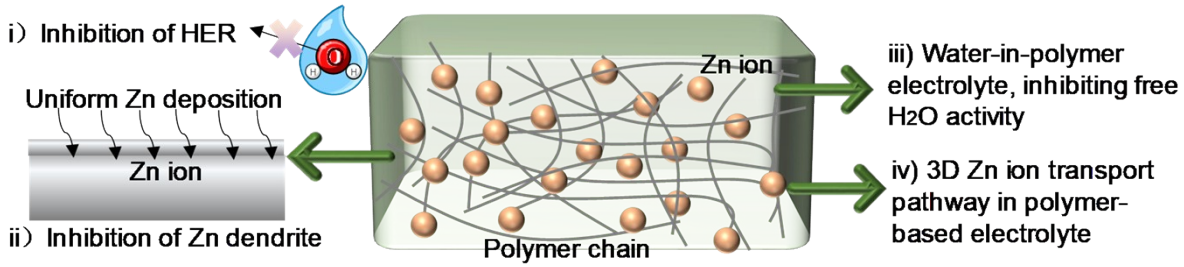

Figure S9. The advantages of Zn ion-MPTS solvation sheaths.

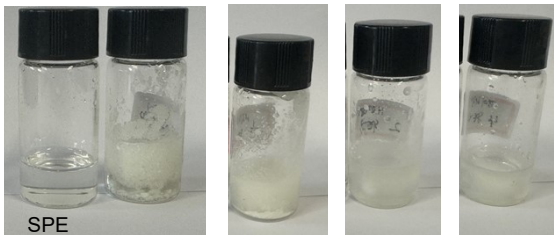

½H_2O: The volume of H_2O becomes half of its original volume.

Figure S10. Digital photos of various electrolytes.

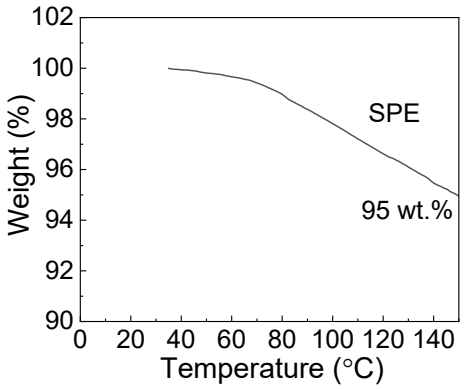

Figure S11. TG result of SPE.

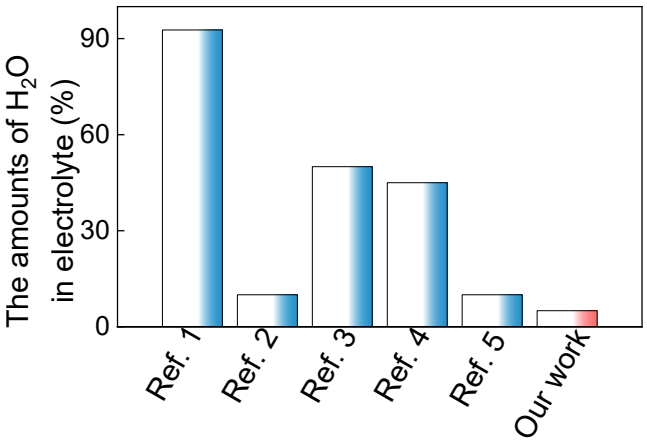

Figure S12. H_2O content in our SPE and other previously reported hydrogel. Ref 1: *ACS Nano*, 2022, 16, 10729; Ref 2: *J. Power Sources*, 2022, 548, 232072; Ref 3: *Nano Lett.*, 2020, 20, 3791; Ref 4: *Chem. Eng. J.*, 2022,434,134646 and Ref 5: *ACS Appl. Mater. Inter.*,2020,1246005.

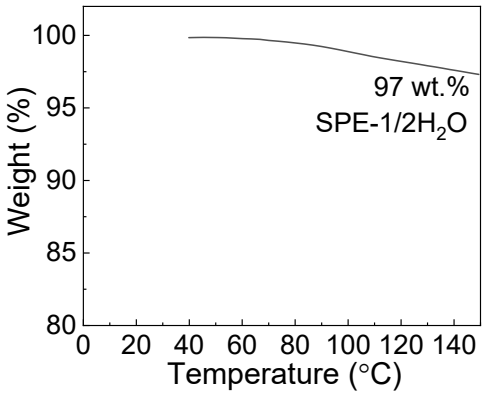

Figure S13. TG result of SPE-1/2H_2O.

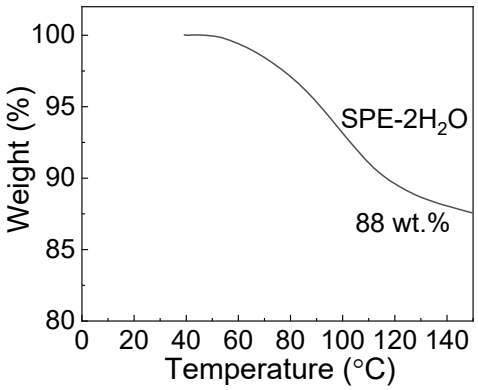

Figure S14. TG result of SPE-2H_2O.

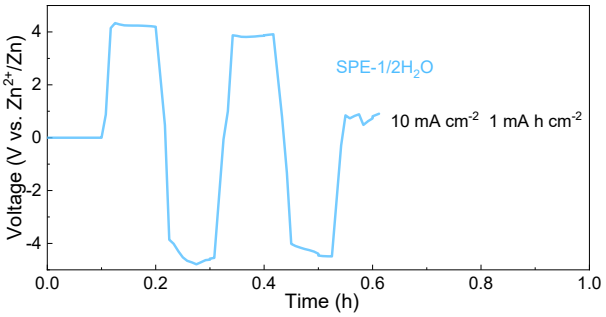

Figure S15. Cycling performances of Zn||Zn symmetrical batteries.

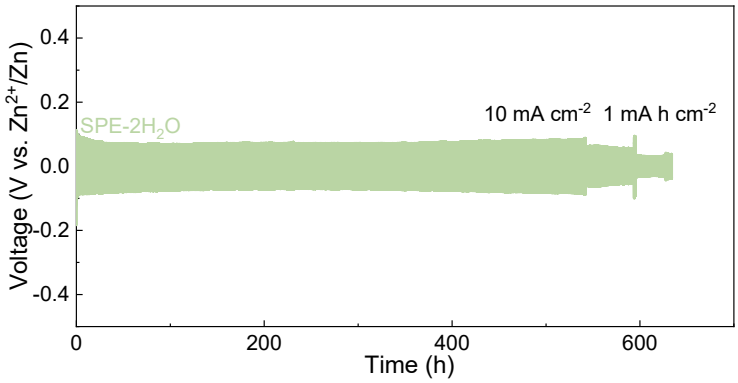

Figure S16. Cycling performances of Zn||Zn symmetrical batteries.

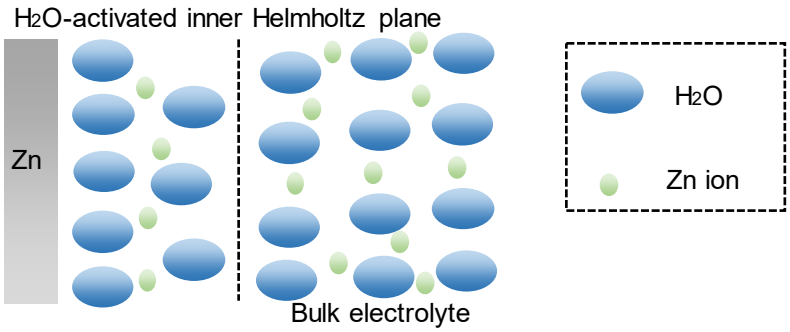

Figure S17. The schematic illustration of the reaction mechanisms of H_2O-activated inner Helmholtz plane.

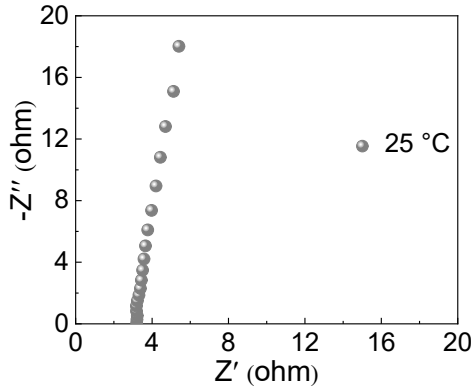

Figure S18. Ionic conductivity of PMPTS-based SPE.

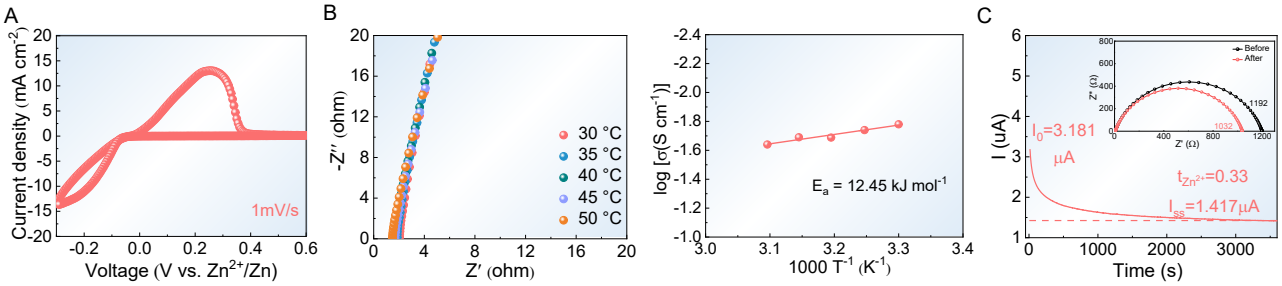

Figure S19. A) CV curve of Zn||PMPTS-based SPE||Cu. B) Ionic conductivity and C) ion transference number of PMPTS-based SPE.

In the cathodic scan, Zn plating on the Cu foil appears at 0.03 V, as shown in **Fig. S19A**. In the subsequent reverse scan, the peak at approximately 0.26 V is assigned to Zn stripping. Because of the presence of soft long side chains (Si-O-CH_3 group), it demonstrates well-interfacial adhesion with the electrode surface,[3, 4] which is beneficial to stable Zn stripping/plating. Additionally, the polymer chain contains only C-C, C-O, C=O, Si-C, and Si-O without any other unstable functional groups, ensuring a wide potential window and good polymer chain stability during cycling.

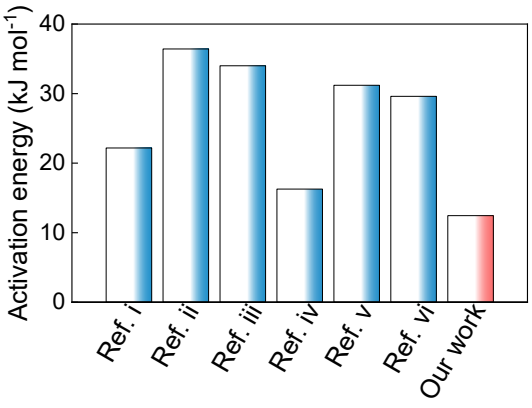

Figure S20. The activation energy of our SPE compared with previous electrolytes.

As shown in **Fig. S20**, the activation energy of Zn ion (12.45kJ mol^{-1}) is lower than that of previous polymer-based electrolytes. Hence, our designed SPE is benefical for the rapid Zn ion movement. The specific data and the releated literatures are listed below. i) 22.18 kJ mol^{-1} for nano-composite polymer electrolytes: (90 PEO: 10 $Zn(CF_3SO_3)_2)^+$ xZnO (*Mater. Today Commun.*, 2017, 13, 269); ii) 36.42 kJ mol^{-1} for polyacrylamide-poly (ethylene glycol) diacrylate-carboxymethyl cellulose hydrogel electrolyte (*Energy Stroage Mater.*, 2022, 49, 172); iii) 34 kJ mol^{-1} for zwitterionic osmolyte-based hydrogel electrolytes (*J. Mater. Chem. A*, 2022, 10, 25701); iv) 16.27 kJ mol^{-1} for polyacrylic acid-containing sol-electrolyte (*eScience*, 2023, 3, 100153); v) 31.2 kJ mol^{-1} for Zn^{2+} ion-exchanged sulfonated poly (ether ketone) (*Energy Stroage Mater.*, 2022, 49, 380); vi) 29.6 kJ mol^{-1} for polycation-regulated electrolyte (*Angew. Chem. Int. Ed.*, 2023, 62, e202302701).

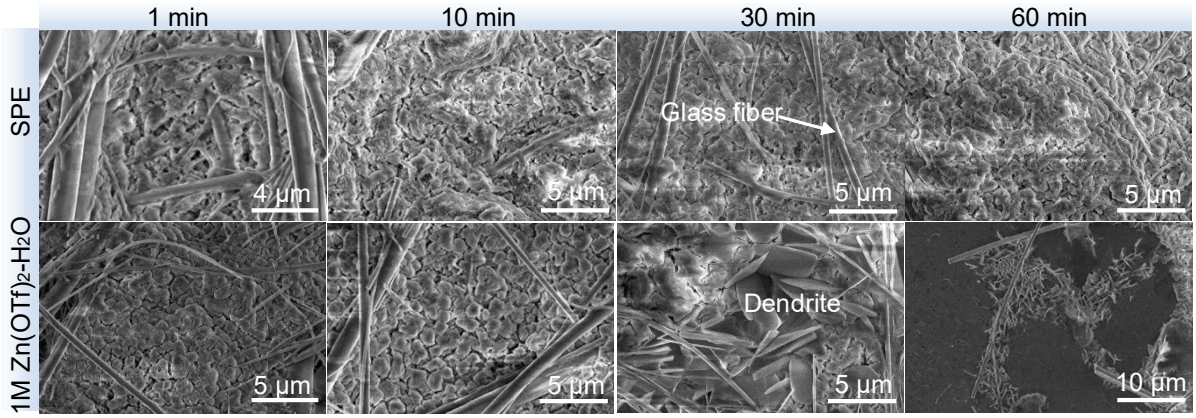

Figure S21. SEM images of Zn deposition with times of 1, 10, 30, and 60 min at a current density of 1 mA cm^{-2} in 1M $Zn(OTf)_2$-H_2O and SPE.

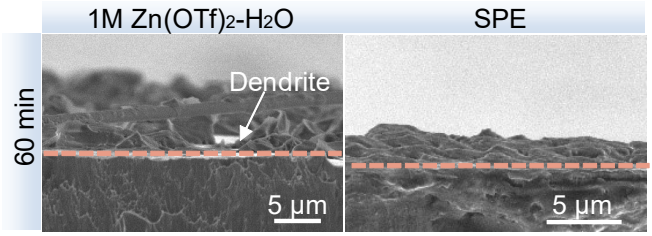

Figure S22. SEM cross-section images of Zn deposition with times of 60 min at a current density of 1 mA cm^{-2} in 1M $Zn(OTf)_2$-H_2O and SPE.

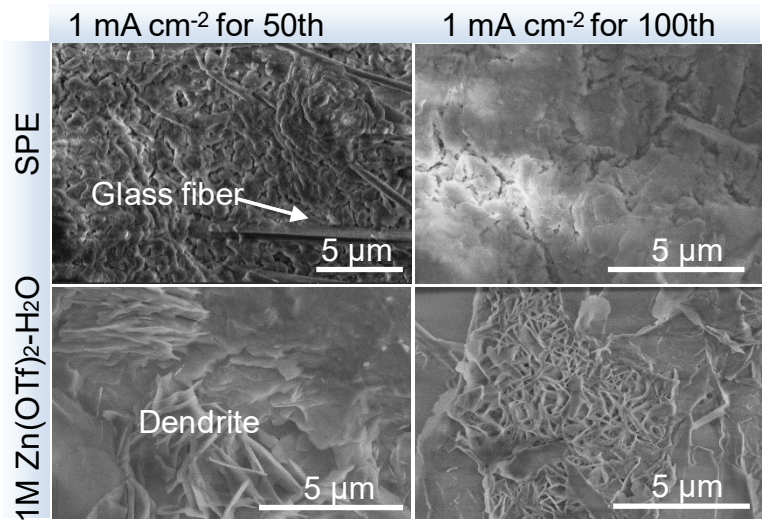

Figure S23. SEM images of Zn deposition at a current density of 1 mA cm^{-2} for various cycles in 1M $Zn(OTf)_2$-H_2O and SPE.

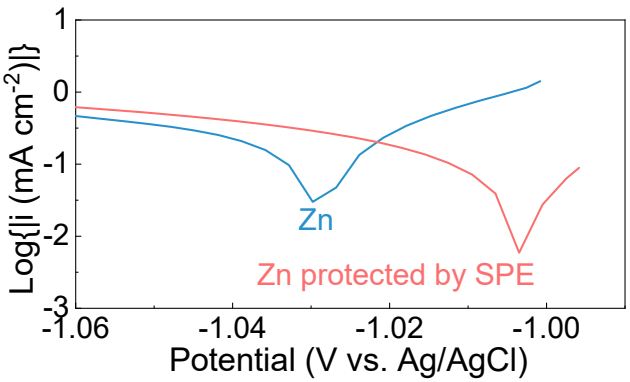

Figure S24. Corrosion curves of various Zn anodes.

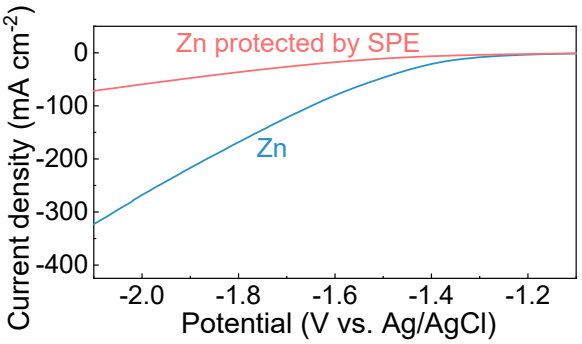

Figure S25. Linear polarization experiments of various Zn anodes.

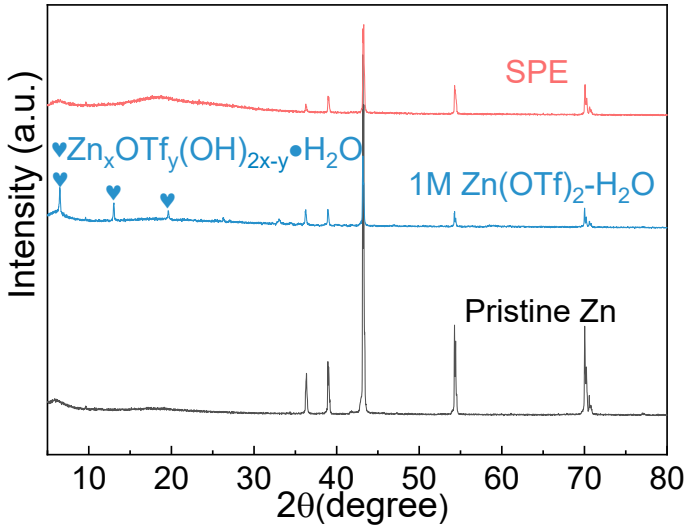

Figure S26. XRD patterns of Zn anodes reobtained from Zn||Zn symmetric cells after 50 cycles.

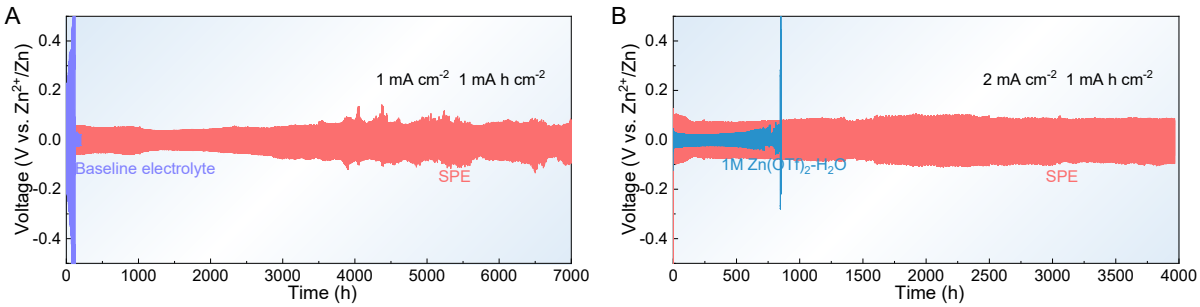

Figure S27. A) Galvanostatic charge-discharge profiles of Zn||Zn symmetrical batteries plating/stripping at 1 mA cm^{-2} for 1 h. B) Galvanostatic charge-discharge profiles of Zn||Zn symmetrical batteries plating/stripping at 2 mA cm^{-2} for 0.5 h.

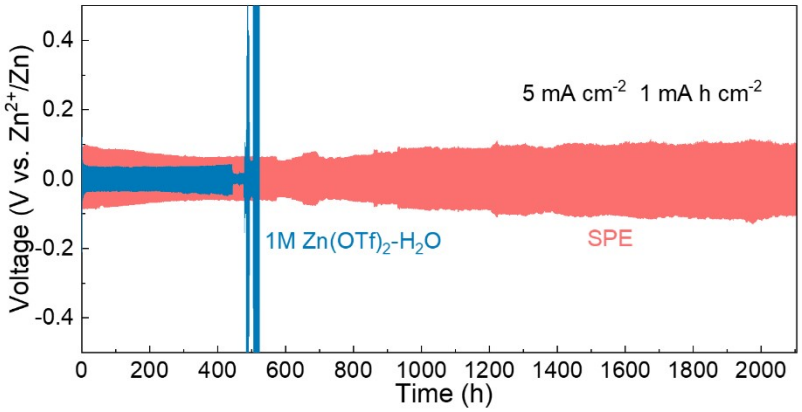

Figure S28. Galvanostatic charge-discharge profiles of Zn||Zn symmetrical batteries plating/stripping at 5 mA cm^{-2} for 12 min. Compared with the $Zn(OTf)_2$-H_2O electrolyte-based symmetric cell, our Zn||SPE||Zn symmetric cell shows a better cycling life and stability at the same condition.

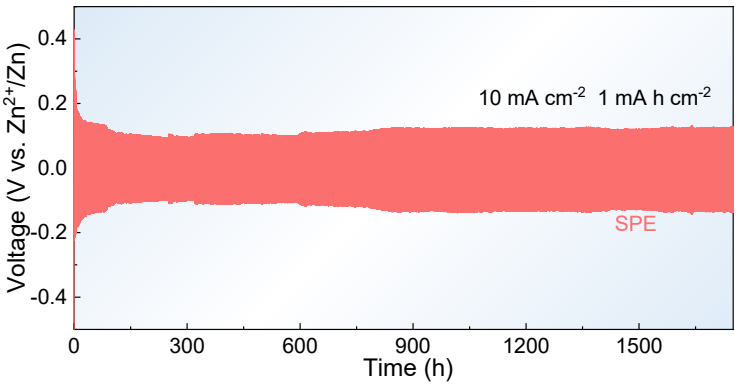

Figure S29. Galvanostatic charge-discharge profiles of Zn||Zn symmetrical batteries plating/stripping at 10 mA cm^{-2} for 6 min.

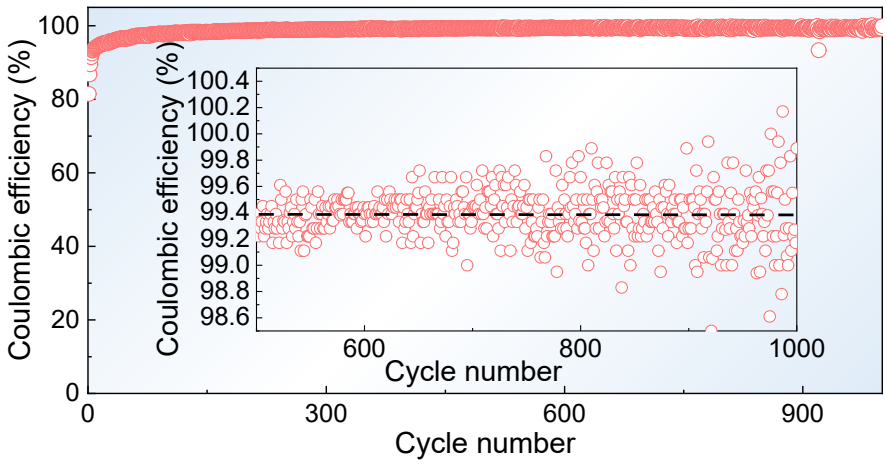

Figure S30. The Zn||Cu asymmetrical batteries at 0.5 mA cm^{-2} for 0.5 mA h cm^{-2}.

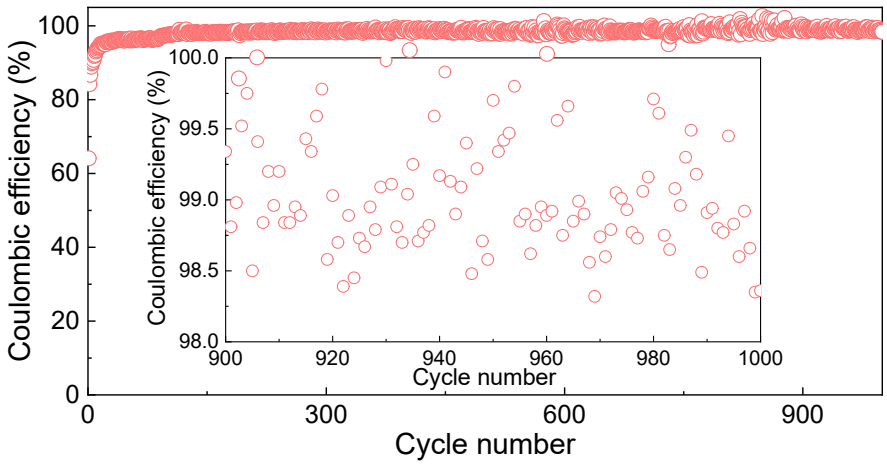

Figure S31. The Zn||Cu asymmetrical batteries for SPE at 1 mA cm^{-2} for 1 mA h cm^{-2}.

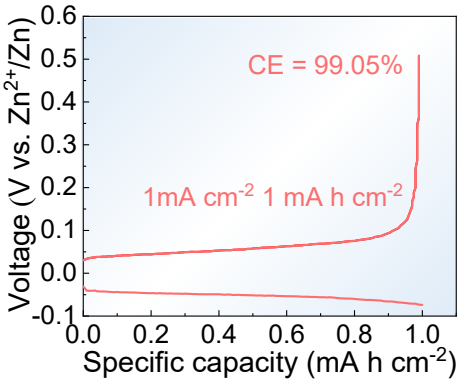

Figure S32. The Zn||Cu asymmetrical batteries for 400th cycle at 1 mA cm^{-2} for 1 mA h cm^{-2}.

.

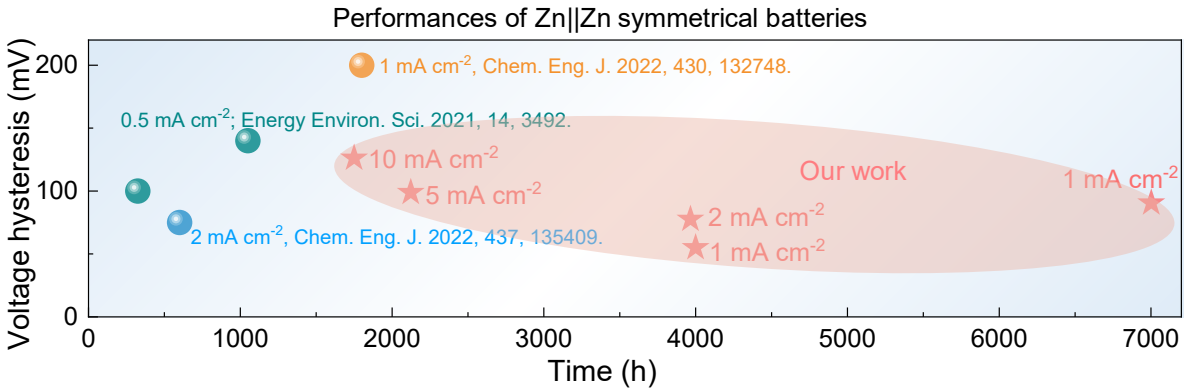

Figure S33. Comparison of cycling performance of Zn||SPE||Zn symmetrical batteries and other reported solid electrolytes.

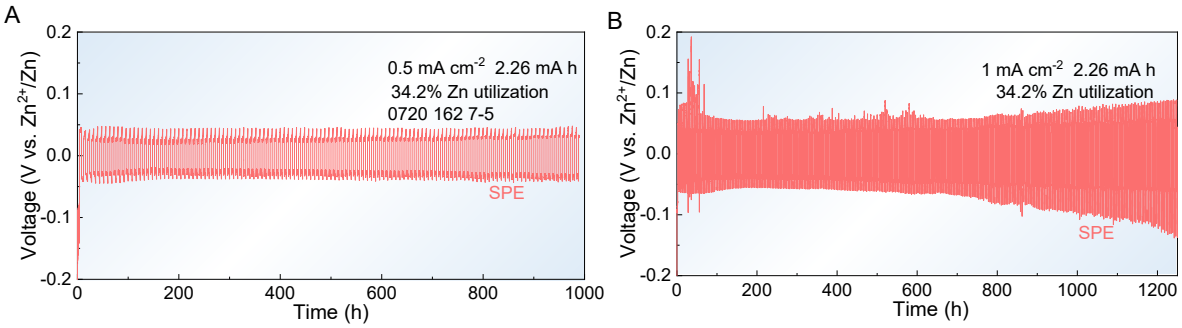

Figure S34. Cycling performances of Zn||SPE||Zn symmetrical batteries at A) 0.5 mA cm^{-2} and B) 1 mA cm^{-2} with a Zn utilization of 34.2%.

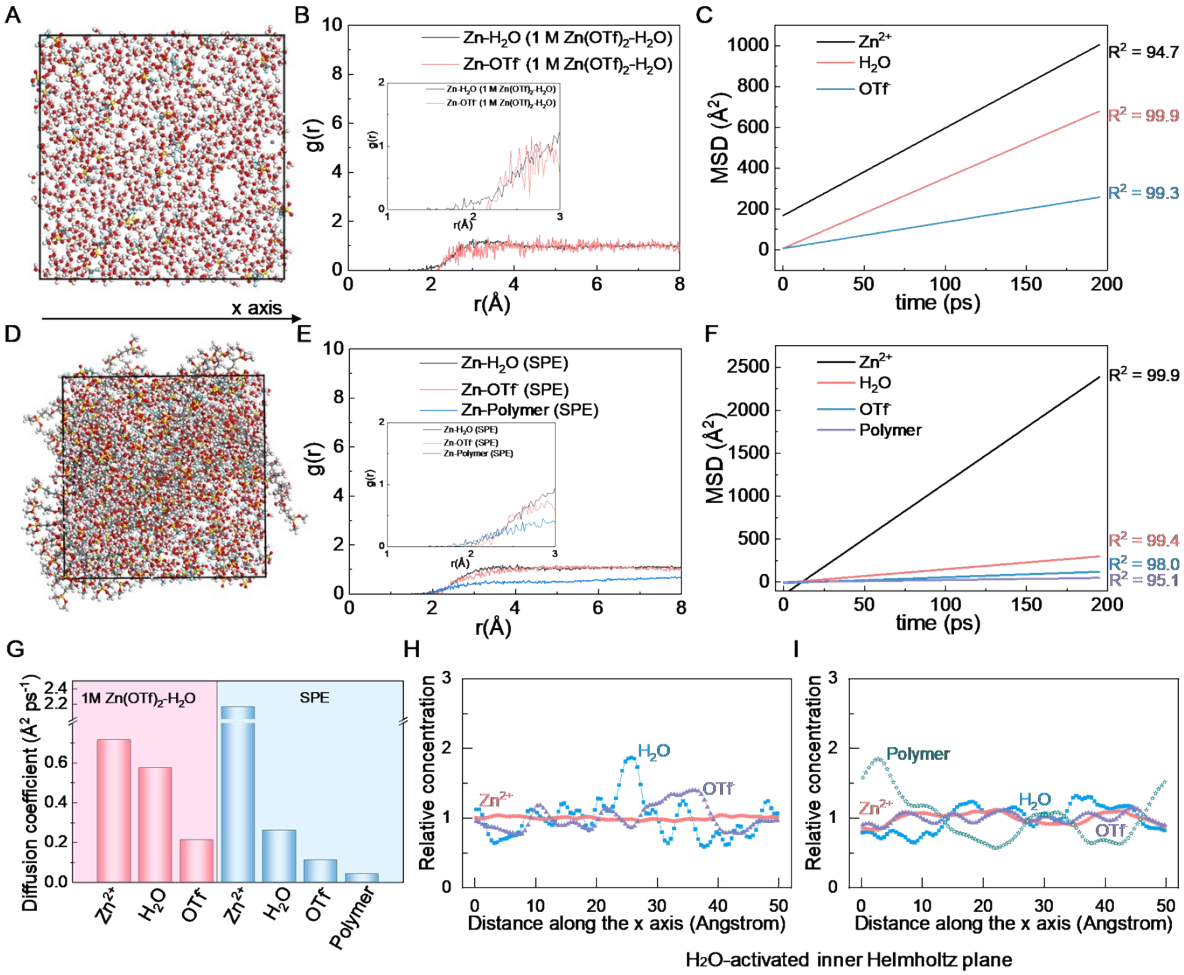

Figure S35. A) 3D snapshots of the simulated solvation structures in 1M $Zn(OTf)_2$-H_2O electrolyte and D) SPE. Radial distribution function [g(r)] obtained from MD simulation of B) 1M $Zn(OTf)_2$-H_2O electrolyte and E) SPE. The average MSD curves obtained from MD simulation of C) 1M $Zn(OTf)_2$-H_2O electrolyte and F) SPE. G) Diffusion coefficient of various components. The relative concentration of various components along the x axis in H) 1M $Zn(OTf)_2$-H_2O electrolyte and I) SPE.

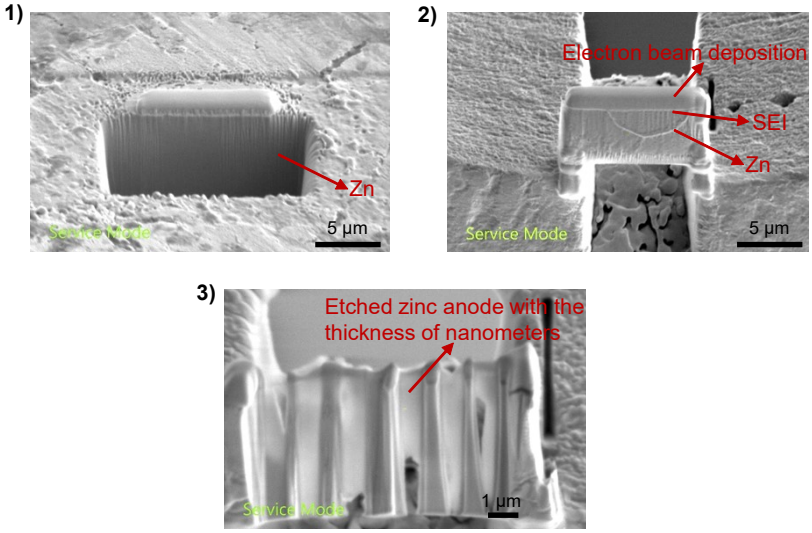

Figure S36. SEM images of the cycled Zn after FIB thinning process for high-resolution TEM (HRTEM) analysis. Specifically, the Zn-metal anode disassembled from the full battery is etched into a cuboid sample with the thickness of 5 μm. Afterwards, the thinning process is carried out unitl the thickness of Zn-metal anode sample is decreased to tens of nanometers. Finally, HRTEM is employed to observe SEI layer of the cycled Zn metal.

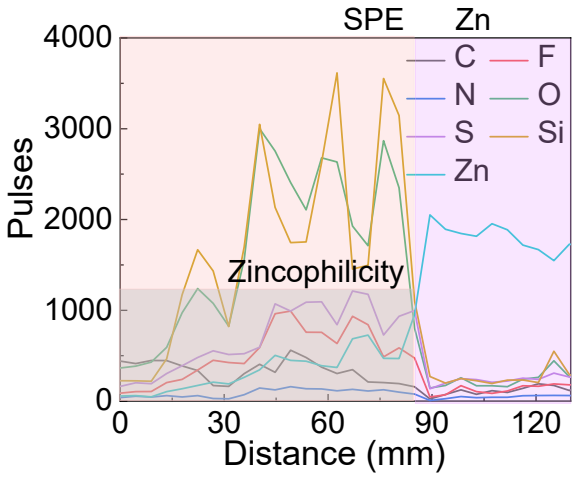

Figure S37. Cross-section SEM line sweep result of SPE/Zn.

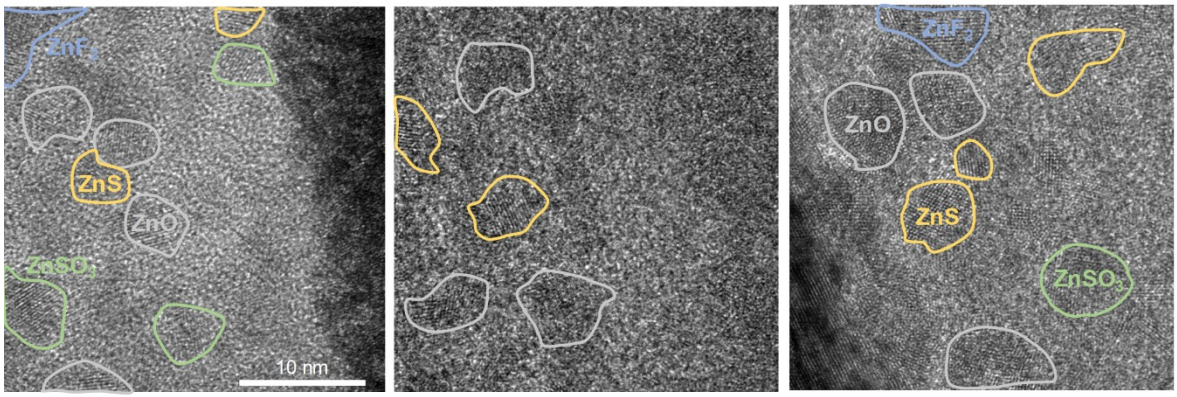

Figure S38. HRTEM images of the cycled Zn in 1M $Zn(OTf)_2$-H_2O electrolyte.

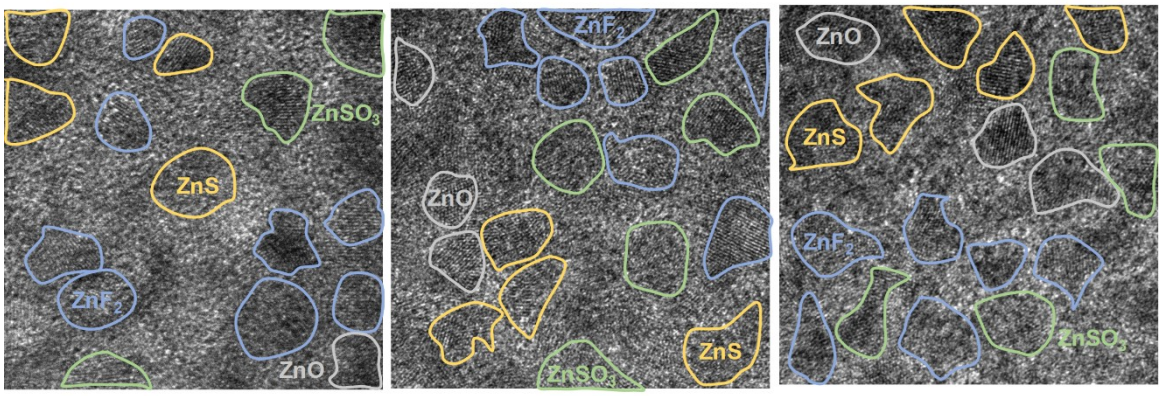

Figure S39. HRTEM images of the cycled Zn in SPE.

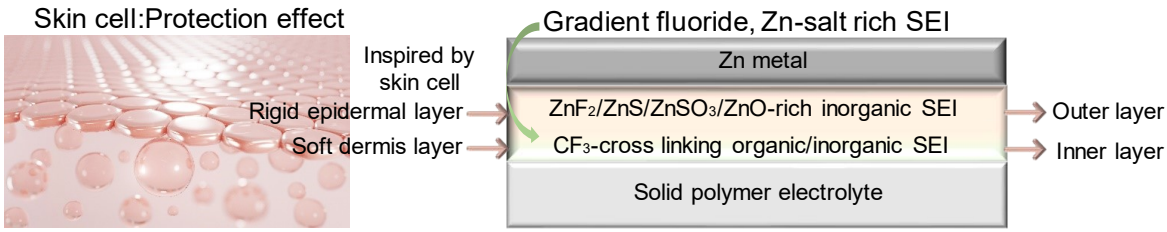

Figure S40. Schematic illustration of our fabricated SEI layer, which is inspired by human skin cell.

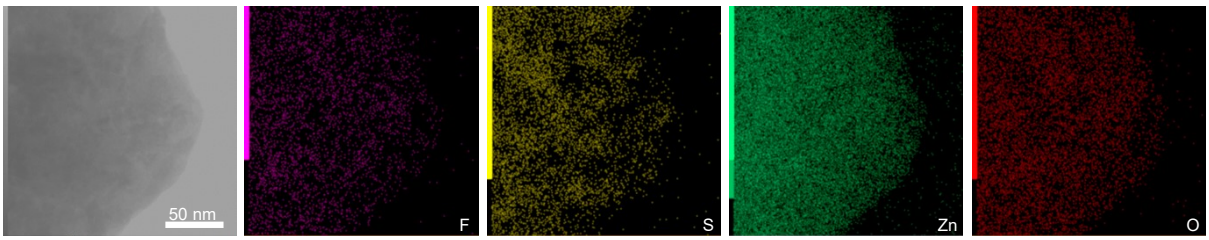

Figure S41. TEM mapping images of the cycled Zn in SPE.

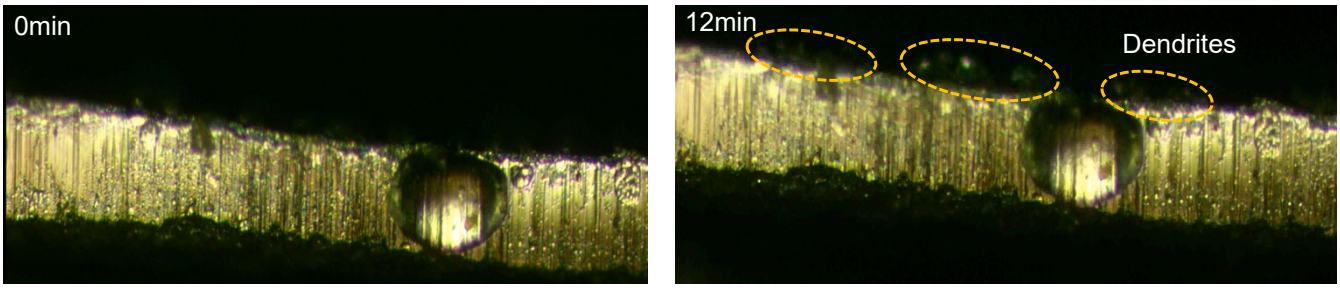

Figure S42. *In situ* optical microscope images of the plated Zn electrode in 1M $Zn(OTf)_2$-H_2O electrolyte.

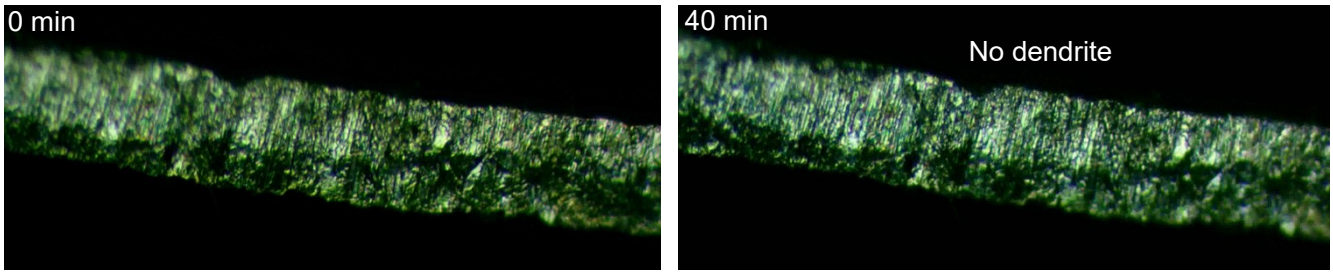

Figure S43. *In situ* optical microscope images of the plated Zn electrode in SPE.

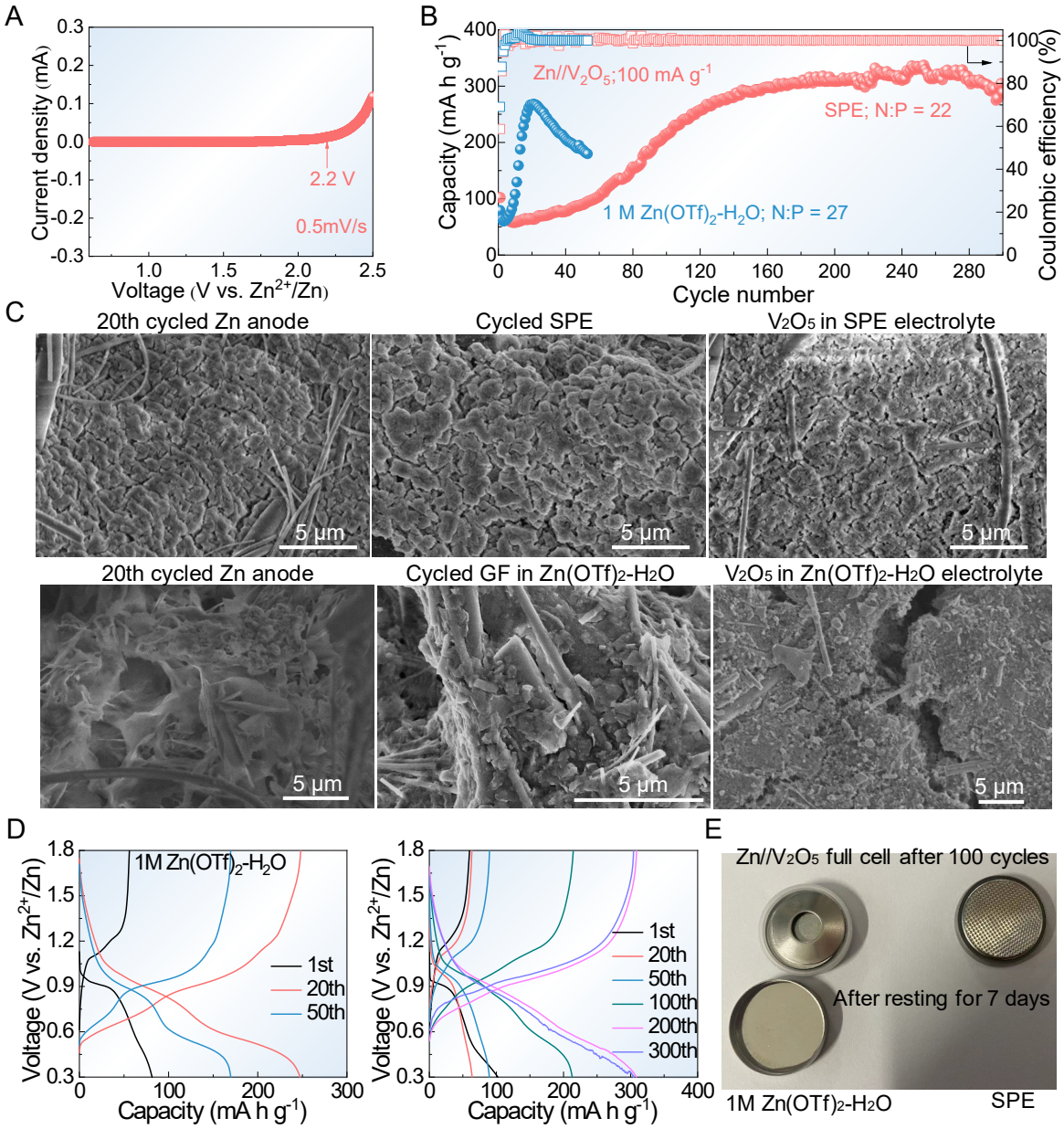

Figure S44. A) Linear sweep voltammetry of Zn||SPE||stainless steel assymmetrical batteries. B) Electrochemical performances of Zn||SPE||V_2O_5 full cell. C) SEM images of Zn, electrolyte and V_2O_5 cathode. D) The galvanostatic discharge-charge curves of Zn//V_2O_5 full cell. E) Optical images of cycled coin cells after 100 cycles.

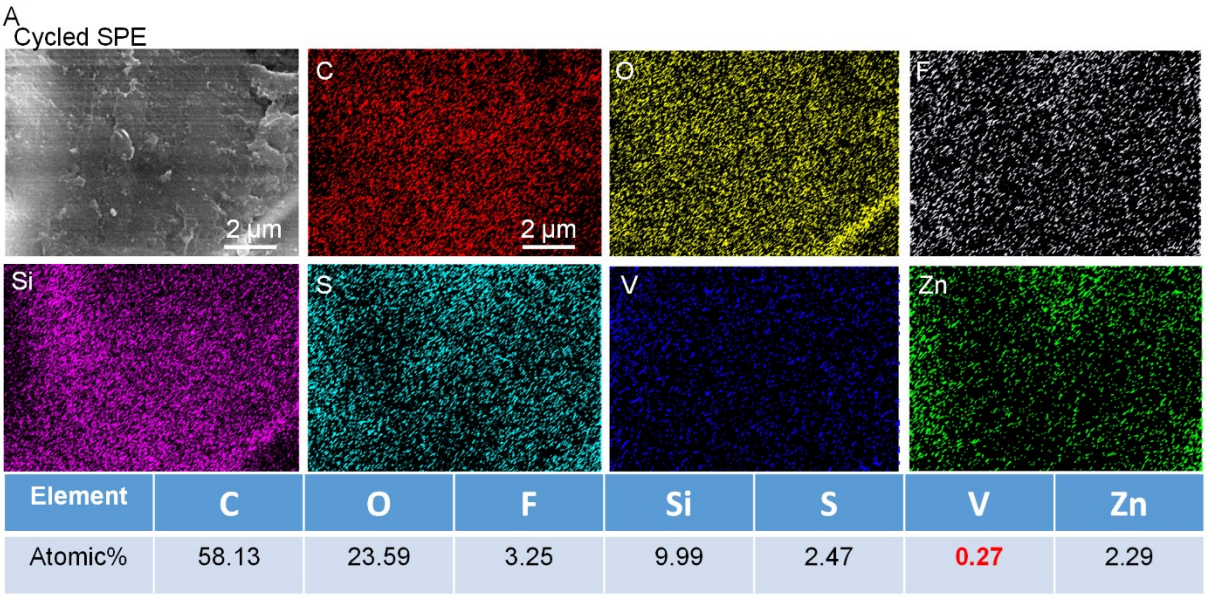

Element	C	O	F	Si	S	V	Zn
Atomic%	58.13	23.59	3.25	9.99	2.47	0.27	2.29

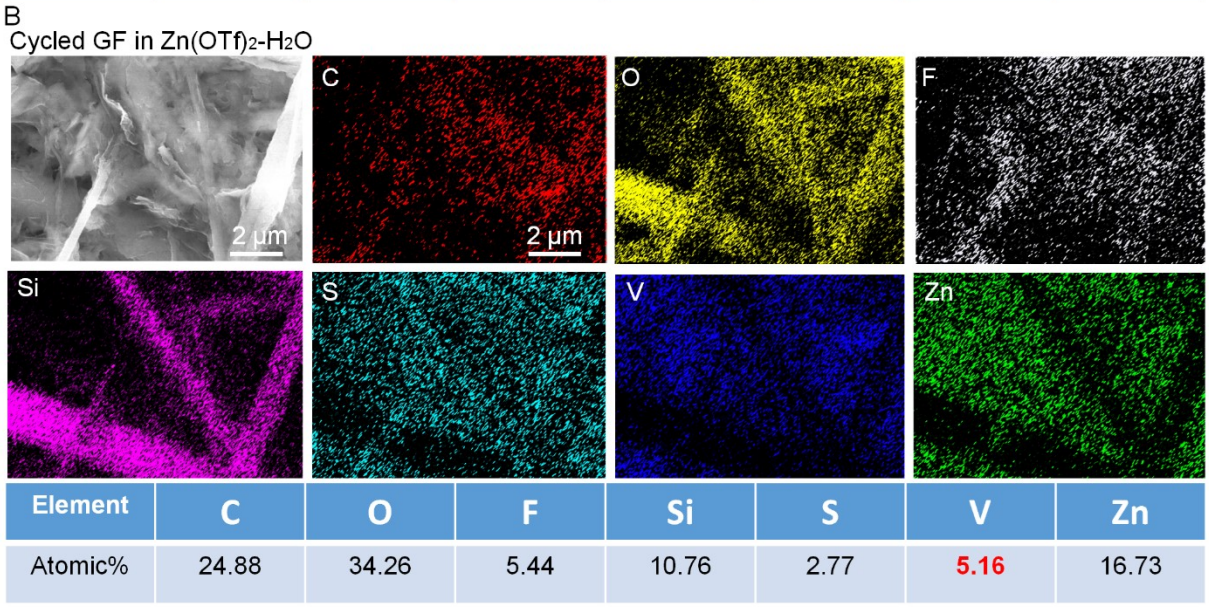

Element	C	O	F	Si	S	V	Zn
Atomic%	24.88	34.26	5.44	10.76	2.77	5.16	16.73

Figure S45. SEM and EDS mapping of various electrolytes after 20 cycles.

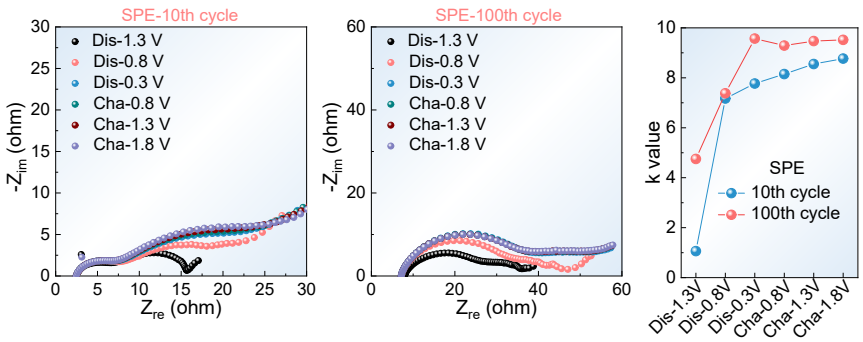

Figure S46. The EIS results of Zn||SPE||V_2O_5 full cell at various discharging/charging voltages.

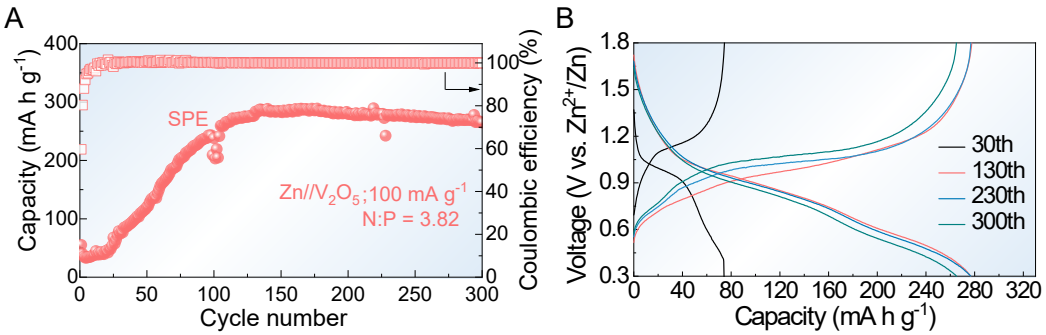

Figure S47. A) Electrochemical performances and B) the galvanostatic discharge-charge curves of Zn//V_2O_5 full cell.

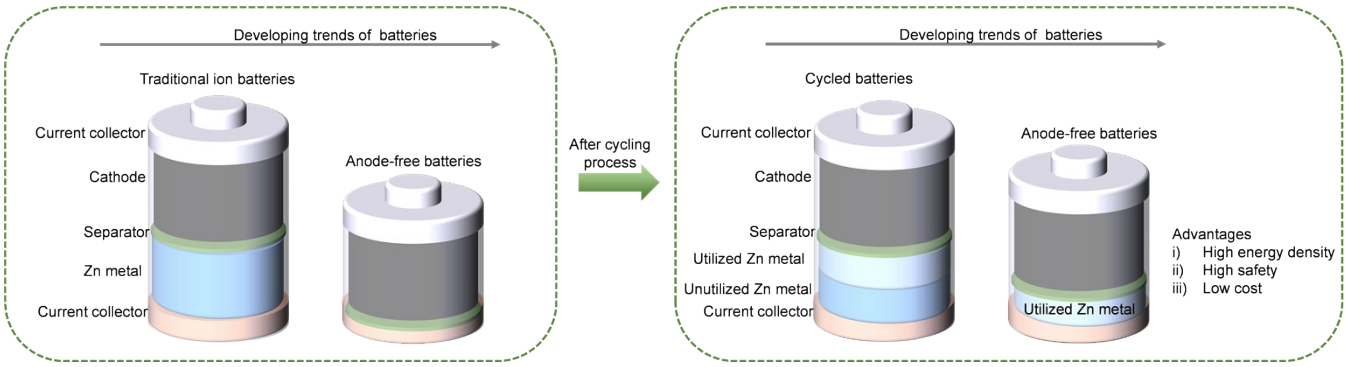

Figure S48. Schematic of configurations of traditional and anode-free cell models.

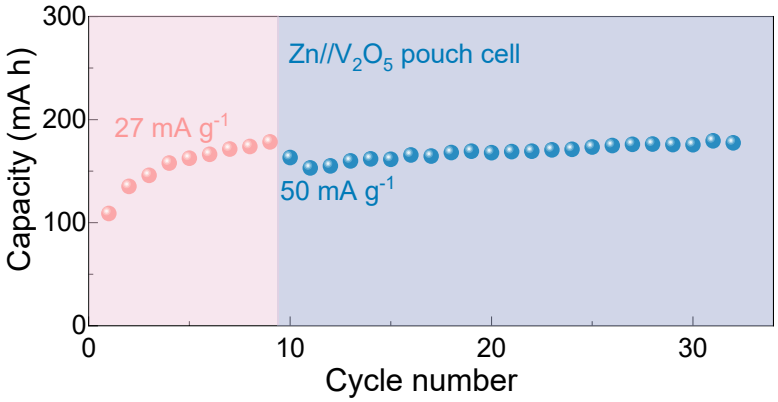

Figure S49. Electrochemical performances of Zn//V_2O_5 pouch cell.

References

1. J.-H. Lee, Y. Byun, G. H. Jeong, C. Choi, J. Kwen, R. Kim, I. H. Kim, S. O. Kim and H.-T. Kim, *Adv. Mater.*, 2019, **31**, 1970366.
2. J. P. Perdew, K. Burke and M. Ernzerhof, *Phy. Rev. Lett.*, 1996, **77**, 3865-3868.
3. W. Zhang, J. Zhang, X. Liu, H. Li, Y. Guo, C. Geng, Y. Tao and Q.-H. Yang, *Adv. Funct. Mater.*, 2022, **32**, 2201205.
4. G. Xi, M. Xiao, S. Wang, D. Han, Y. Li and Y. Meng, *Adv. Funct. Mater.*, 2021, **31**, 2007598.